

## The Mass of Stirring Bodies in the AU Mic Debris Disk inferred from Resolved Vertical Structure

CAIL DALEY,<sup>1</sup> A. MEREDITH HUGHES,<sup>1</sup> EVAN CARTER,<sup>1</sup> KEVIN FLAHERTY,<sup>1</sup>  
ZACHARY LAMBROS,<sup>1</sup> MARGARET PAN,<sup>2</sup> HILKE SCHLICHTING,<sup>3,2</sup> MARK WYATT,<sup>4</sup>  
EUGENE CHIANG,<sup>5,6</sup> DAVID WILNER,<sup>7</sup> SEAN ANDREWS,<sup>7</sup> AND JOHN CARPENTER<sup>8</sup>

<sup>1</sup>*Department of Astronomy, Van Vleck Observatory, Wesleyan University, 96 Foss Hill Drive, Middletown, CT 06459, USA*

<sup>2</sup>*Department of Earth, Atmospheric and Planetary Sciences, Massachusetts Institute of Technology, Cambridge, MA 02139, USA*

<sup>3</sup>*Department of Earth and Space Sciences, University of California, Los Angeles, CA 90095, USA*

<sup>4</sup>*Institute of Astronomy, University of Cambridge, Madingley Road, Cambridge CB3 0HA, United Kingdom*

<sup>5</sup>*Department of Astronomy, University of California at Berkeley, Campbell Hall, Berkeley, CA 94720-3411*

<sup>6</sup>*Department of Earth and Planetary Science, University of California at Berkeley, McCone Hall, Berkeley, CA 94720-3411*

<sup>7</sup>*Harvard-Smithsonian Center for Astrophysics, 60 Garden Street, Cambridge, MA, 02138, USA*

<sup>8</sup>*Joint ALMA Observatory (JAO), Alonso de Cordova 3107 Vitacura-Santiago de Chile, Chile*

### ABSTRACT

The vertical distribution of dust in debris disks is particularly sensitive to the total mass of planetary bodies stirring the disk, and is therefore well suited for constraining the prevalence of otherwise unobservable Uranus and Neptune analogs. Inferences of dynamical mass from debris disk vertical structure have previously been applied to infrared and optical observations of several systems, but the small particles traced by short-wavelength observations are ‘puffed up’ by radiation pressure, yielding only upper limits on the total dynamical mass. The large grains that dominate the emission at millimeter wavelengths are much less sensitive to the effects of stellar radiation, and therefore trace the underlying mass distribution more directly. Here we present ALMA 1.3 mm dust continuum observations of the debris disk around the nearby M star AU Mic. The 3 au spatial resolution of the observations, combined with the favorable edge-on geometry of the system, allows us to measure the vertical structure of the disk; we report a scale height-to-radius aspect ratio of  $h = 0.031 \pm 0.005$

between  $\sim 24$  au and  $\sim 42$  au. Comparing the observed aspect ratio to a theoretical model of steady-state, size-dependent velocity distributions in the collisional cascade we estimate the total mass of bodies stirring the disk to be  $\sim 1.5 M_{\oplus}$ . These measurements rule out the presence of a gas giant or Neptune analog near the outer edge of the disk, but are suggestive of the presence of large planetesimals or an Earth-sized planet stirring the dust distribution.

## 1. INTRODUCTION

Planets form during a relatively short and early stage in the lifetime of stellar systems, when the host star is still encircled by a protoplanetary disk rich in gas. Planet formation (as well as processes including accretion, photoevaporation, and winds) causes first-generation protoplanetary material to dissipate over time (Williams & Cieza 2011; Ercolano & Pascucci 2017). The first-generation material is replaced by second-generation ‘debris,’ produced by a collisional grinding of larger planetesimals into small dust grains in a process known as a collisional cascade (Wyatt 2008). The resulting debris disks, optically thin and significantly less luminous than their protoplanetary counterparts, are found around at least 25% of Solar-type stars and are likely to be as common as the exoplanetary systems with which they are thought to be associated (Montesinos et al. 2016).

Analysis of the morphological and emissive properties of debris disks sheds light on the final stages of planetary system evolution and can reveal the presence of planets hidden within. Planets can imprint features such as rings/gaps, clumps, or other asymmetries on their parent disks, although it is rarely straightforward to infer the properties of planets directly from the disk morphology (see the review by Hughes et al. 2018, and references therein). In gas-poor systems, the vertical structure of a debris disk can serve as a probe of the total mass of large bodies stirring the collisional cascade (Thébault 2009). The presence of massive bodies increases the inclination dispersion of the dust particle orbits and thus the scale height  $H$  of the observed dust distribution.

The dynamical excitation of a disk can therefore be measured from its aspect ratio  $H/r$ , which in turn allows inferences about the presence and size of the bodies responsible for the dynamical stirring. Such work has been undertaken by several authors using visible and infrared observations (Artymowicz 1997; Thébault & Augereau

2007; Quillen et al. 2007). However, Thébault (2009) demonstrate that radiation pressure from the host star should preferentially excite the smallest dust grains in the disk, imparting a ‘natural’ scale height even in the absence of large bodies dynamically stirring the disk. Thus longer-wavelength ( $\lambda \geq 50 \mu\text{m}$  for typical grain blow-out sizes of  $\sim 2 - 10 \mu\text{m}$ ) observations are required to measure the disk scale height as determined by dynamical stirring alone, since the large grains dominating the emission at these wavelengths are much less sensitive to the effects of radiation pressure.

The M3IVe star AU Mic presents a particularly favorable target for such observations due to its proximity ( $9.725 \pm 0.005 \text{ pc}$ ; Gaia Collaboration et al. 2016, 2018), edge-on inclination, and apparently symmetric morphology at millimeter wavelengths. The first M star detected to have a far-infrared excess, AU Mic hosts one of the best-studied debris disks (Moshir et al. 1990). As a member of the  $\beta$  Pic Moving Group, it is thought to be relatively young:  $23 \pm 2 \text{ Myr}$  (Binks & Jeffries 2014; Mamajek & Bell 2014; Malo et al. 2014). The disk around AU Mic was first resolved by Kalas et al. (2004) in scattered light, and a host of observations spanning the optical to the submillimeter have followed (Augereau & Beust 2006; MacGregor et al. 2013; Matthews et al. 2015; Schneider et al. 2014; Wang et al. 2015). Notably, the debris around AU Mic exhibits a so-far-unique time variability at scattered light wavelengths. Boccaletti et al. (2015) and Boccaletti et al. (2018) identify several local intensity maxima offset from the disk midplane on the southeast side of the disk. These features are moving quickly away from the star along the disk midplane at projected velocities that are not consistent with Keplerian rotation; in fact, the outermost features appear to be unbound from the star (see also Sezestre et al. (2017) who provide kinematic fits and invoke a dust source of unspecified nature). Chiang & Fung (2017) propose that these fast-moving features are dust particles repelled by a time-variable stellar wind that triggers dust avalanches when the wind blows strongest. These avalanches are seeded by the debris remaining from the recent disruption of a  $\sim 400\text{-km}$  sized progenitor. In this paper we will provide an independent constraint on the presence of comparably sized planetesimals.

We present here new  $0.3''$  Atacama Large Millimeter/submillimeter Array (ALMA)  $1.3 \text{ mm}$  observations of the AU Mic debris disk. These observations represent a factor of  $\sim 2$  improvement in both spatial resolution and rms noise relative to previous ALMA observations of the system by MacGregor et al. (2013), and our anal-

ysis indicates that the vertical structure of the disk is resolved with  $4\sigma$  confidence. In §2 we present the new observations and describe the data reduction. Section 3 documents the basic observational results regarding the disk flux, morphology, and gas content. In §4 we conduct a parametric exploration of a 2-dimensional disk model in order to investigate the degeneracy between vertical structure, radial structure, and viewing geometry. In §5 we discuss our results, particularly the constraints on the dynamical excitation of the disk imposed by our measurement of the scale height, and compare them to previous observations. The results of our measurement of scale height and its implications for the total disk mass are summarized in §6.

## 2. OBSERVATIONS

AU Mic was observed with ALMA on three dates: 26 March 2014, 18 August 2014, and 24 June 2015 (see Table 1). All observations employed ALMA’s 12m antennas and Band 6 receivers, including four independently tunable spectral windows each with a bandwidth of 1.875 GHz. One spectral window was centered around the CO  $J = 2 - 1$  transition at a rest frequency of 230.538001 GHz and a channel spacing of 0.6 km/s. The remaining three spectral windows were configured to detect continuum emission with channel spacings of 21.7 km/s and central frequencies of 228.5, 213.5, and 216.0 GHz. The mean of the four central wavelengths is 1.3 m. The baseline lengths range between 12 m and 1320 m; the longest baseline among the three observations traces an angular scale of  $0.22''$  and a spatial scale of 2.1 au.

Calibration, reduction, and imaging were carried out using the **CASA** (McMullin et al. 2007) software package. Standard ALMA reduction scripts were applied to the datasets: phase calibration was accomplished via gain calibration and water vapor radiometry tables, while system temperature calibrations were performed to account for variations in instrument and weather conditions. Flux and bandpass calibrations were subsequently applied; the flux calibration is subject to a 10% systematic uncertainty. In addition to these standard procedures, the weights of the visibilities were recalculated using the variance around each baseline as in Flaherty et al. (2017).

During the last segment of the June observation (04:23:38–04:29:58 UT), the host star flared. To determine the flux of the flare as a function of time, we binned the data into one-minute intervals using the **CASA** task `split` and fit a point source in each bin to baselines between 100 k $\lambda$  and 1400 k $\lambda$  with `uvmodelfit`. The resulting point-source fits can be found in Table 2. We exclude from our analysis of the disk

Observational parameters	26 March 2014	18 August 2014	24 June 2015
Antennas:	32	35	37
Baseline length (m):	12–406	19–1160	30–1320
On-source time (min):	35	35	33
Flux calibrator:	Titan	J2056-472	Titan
Bandpass calibrator:	J1924-2914	J2056-4714	J1924-2914
Gain calibrator:	J2101-2933	J2101-2933	J2056-3208
pwv range (mm):	[0.63, 0.66]	[1.58, 1.69]	[0.67, 0.74]
Imaging parameters			
Beam size (arcsec):	$1.27 \times 0.74$	$0.33 \times 0.30$	$0.47 \times 0.31$
Peak intensity ( $\mu\text{Jy}/\text{beam}$ ):	630	240	320
rms noise ( $\mu\text{Jy}/\text{beam}$ ):	30	30	20

**Table 1.** Observational and imaging parameters for the three datasets used in this work. Images were created using the **CASA** task **tclean** with natural weighting.

Time (UTC)	Point-source Flux (mJy)
03:45:0–04:20:0 (no flare)	$0.41 \pm 0.02$
4:23:38–4:24:00	$0.92 \pm 0.17$
4:24:00–4:25:00	$11.46 \pm 0.10$
4:25:00–4:26:00	$3.59 \pm 0.10$
4:26:00–4:27:00	$1.58 \pm 0.10$
4:27:00–4:28:00	$0.45 \pm 0.10$
4:28:00–4:29:00	$0.46 \pm 0.10$
4:29:00–4:29:58	$0.52 \pm 0.10$

**Table 2.** Central point source flux before and during the June 24 flare

emission the seven minutes during which the flare occurred, as it proved difficult to separate the stellar emission from the disk emission while it was changing so rapidly.

Since AU Mic is a high proper motion system, its equatorial coordinates changed significantly over the 1.5 years between first and last observations. We were able to obtain a more precise alignment of the datasets from the bright chromospheric emission of the central star than from the measured proper motion. We fit an image-domain elliptical Gaussian to a small region around the star on each date with the task **imfit**, and used the centroid of the Gaussian fit to define the star position. Each

dataset was then phase-shifted using the task `fixvis` so that the pointing center of the data was the same as the fitted star position. We note that the exclusion of the flare changed the centroid of the Gaussian fit for the June observations by  $0.690 \pm 0.018$  au (18% of the synthesized beam) although the errors reported here, derived from the `imfit` uncertainties, are a factor of five smaller than those given by the ratio of beam size to SNR. This change in the fit stellar location could be explained if the flare were not symmetric with respect to the star.

Imaging was performed using standard Fourier inversion methods as implemented in the `CASA` task `tclean`. Two weighting schemes were used: (i) natural weighting with no taper to trace the small-scale disk structure and (ii) natural weighting with a  $200\text{ k}\lambda$  Gaussian taper applied to long baselines to bring out the disk emission on larger spatial scales. In scheme (i) the rms noise  $\sigma$  was  $15\text{ }\mu\text{Jy/beam}$  and the restoring beam was  $0.52'' \times 0.39''$  with a position angle (PA) of  $77^\circ.9$ . In scheme (ii), the corresponding values are  $20\text{ }\mu\text{Jy/beam}$ ,  $0.87'' \times 0.71''$ , and  $80^\circ.8$ . Because the `CASA` task `tclean` preserves pointing center offsets when converting several visibility datasets into an image, it was necessary to combine the data into a single file before cleaning with the task `concat` in order to account for the offset in phase center between datasets.

### 3. RESULTS

Figure 1 shows the combined dust continuum emission from all three observations at  $1.3\text{ mm}$ ; chromospheric emission from the M star is visible as a point source at the center of the image (Cranmer et al. 2013). The peak signal-to-noise ratio of dust emission is  $\sim 23$ . Using the `MIRIAD` task `cgcurs` (Sault et al. 1995), we measure an integrated flux of  $4.97 \pm 0.08\text{ mJy}$  enclosed within the  $3\sigma$  contours of the naturally weighted image. We note that this value represents the combined emission from the disk *and* the star. Faithfully disentangling the two components proved difficult, both because the stellar flux varied significantly across the three nights of observation (Table 3) and because emission from the star and edge-on disk overlap in the sky plane. Consequently, the most accurate way to isolate the disk flux from the stellar contribution is through parametric modeling (see §4) where the two components can be specified separately; our modeling yields a disk flux of  $4.80 \pm 0.17\text{ mJy}$ .

The ansa to the NW exhibits a maximum flux density of  $330 \pm 15\text{ }\mu\text{Jy/beam}$  at a separation of  $24.1 \pm 0.2\text{ au}$  and PA of  $128^\circ.2 \pm 0.4$ , while the ansa to the SE exhibits a maximum flux density of  $340 \pm 15\text{ }\mu\text{Jy}$  at a separation of  $29.0 \pm 0.2\text{ au}$  and PA

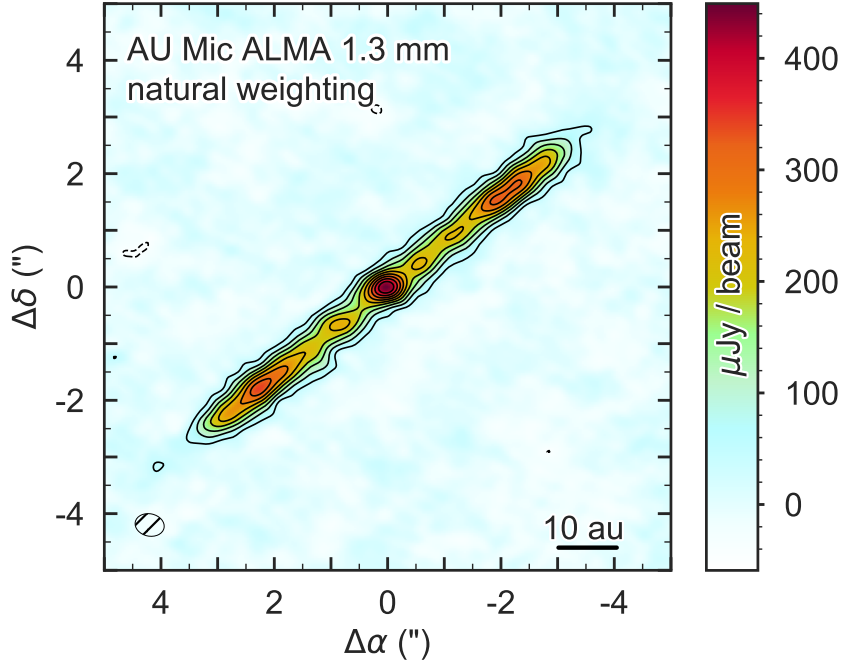


**Figure 1.** The AU Mic system imaged by ALMA at a wavelength of 1.3 mm, using natural weighting with and without a Gaussian taper on the long baselines. For the untapered weighting, the rms noise is  $15 \mu\text{Jy}/\text{beam}$  and the restoring beam has dimensions  $0.52'' \times 0.39''$  with a PA of  $77^\circ.9$ . The corresponding values for the tapered weighting are  $20 \mu\text{Jy}/\text{beam}$ ,  $0.87'' \times 0.71''$ , and  $80^\circ.8$ . Contours are integer multiples of the three times the rms noise. The hatched ellipse in the bottom left of each pane designates the size and shape of the restoring beam.

of  $128^\circ.7 \pm 0.4$ . Here PA is measured counterclockwise with respect to the north celestial pole. The discrepancy in position angle between the two peaks falls within the estimated uncertainties and so we are not able to confirm the scattered light PA offset observed by [Boccaletti et al. \(2015\)](#). The peak flux densities of the ansae

differ by less than the rms noise, indicating that there is no significant difference in brightness between the two sides of the disk. Indeed, the apparent flux asymmetry in these data is in the opposite direction of the apparent flux asymmetry in [MacGregor et al. \(2013\)](#), providing further circumstantial evidence that there is no significant flux asymmetry at millimeter wavelengths.

While comparison of the ansae peak flux densities suggests that the AU Mic disk does not exhibit severe asymmetry, a more detailed analysis can be conducted by extracting surface brightness and vertical structure profiles from the naturally weighted image in Figure 1. These profiles, shown in Figure 2, were created by fitting a one-dimensional Gaussian to the disk vertical surface brightness profile at a series of stellocentric separations along the disk major axis. The top, center, and bottom panes correspond respectively to the amplitude, centroid, and beam-subtracted FWHM of the Gaussian fits. Broadening effects of the synthesized beam in the vertical direction have been removed by subtracting in quadrature the Gaussian beam FWHM from the Gaussian fit FWHM. In more physical terms, the three panes represent the intensity at the location of the disk “spine,” the spine’s elevation from the midplane, and the disk FWHM.

As seen in the top pane of Figure 2, the surface brightness profiles of the two ansae generally mirror each other. However, we note the presence of slightly asymmetric local intensity maxima in the inner regions of the disk, one  $\sim 10.5$  au to the SE of the star and one  $\sim 7.3$  au to the NW. It is unclear whether these are real features of the disk or artifacts of the rms noise or cleaning process; we examine the significance of these features in §4. Three-sigma emission as determined from the surface brightness profile extends to a radial distance of  $\sim 42$  au on the NW side and  $\sim 44$  au on the SE side. Thus, the disk is resolved across  $\sim 17$  beams along the major axis. cursory analysis indicates the disk is marginally resolved perpendicular to the major axis as well, exhibiting a vertical FWHM of  $2.8 \pm 0.5$  au  $\approx 2/3$  beam after taking into account the broadening effects of the beam (see Figure 2, bottom pane). Our ability to resolve the vertical structure of the AU Mic debris disk is discussed in greater detail in §5.6. We were unable to detect (in either the combined dataset or the three individual epochs) the intensity variations or excursions of the disk spine from the midplane that characterize the fast-moving features observed by [Boccaletti et al. \(2015, 2018\)](#). This is not entirely surprising, as both [Sezestre et al. \(2017\)](#) and



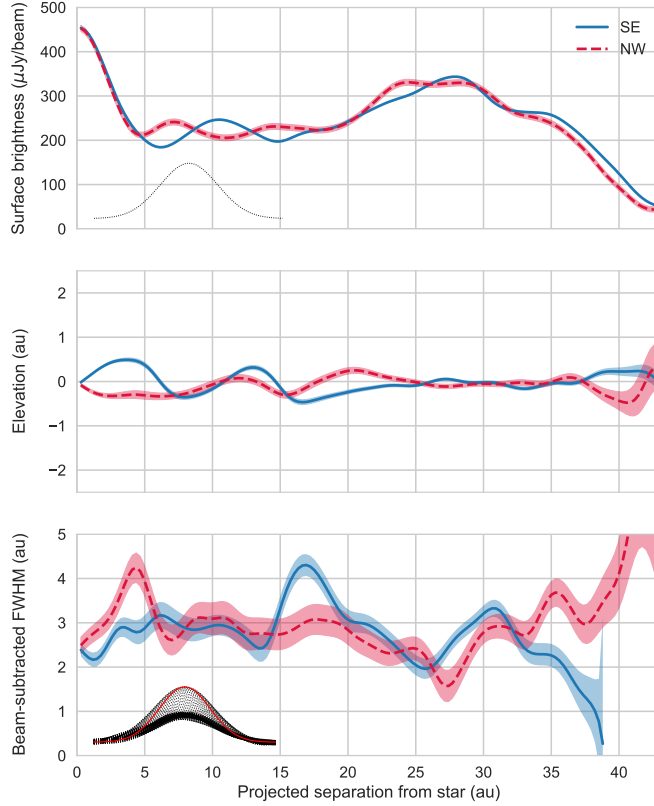


**Figure 2.** The AU Mic debris disk’s radial and vertical structure, extracted from the naturally weighted image in Figure 1. The solid blue line shows the southeast limb of the disk, while the dashed red line shows the northeast limb. From top to bottom, the three panes show i) the disk spine surface brightness with errors given by the rms noise, ii) the disk spine deviation from the midplane, and the disk FWHM as a function of projected separation from the star after subtraction of the beam FWHM in the vertical direction. The Gaussian traced by the dotted line in the first pane shows the projected width in the radial direction of the naturally weighted synthesized beam of the combined dataset; note that this is slightly larger than the projected width in the vertical direction. Although the last pane indicates a beam-subtracted disk FWHM that is technically smaller than the vertical FWHM of the beam, the fact that the image-domain vertical height of the disk is consistently in excess of the beam contribution in regions of high signal-to-noise implies that our data spatially resolve the vertical structure of the disk. Our the significance of our measurement of the scale height is discussed further in §4.3. Because the disk is viewed edge-on and a wide range of stellocentric separations contribute to the FWHM at a given projected separation, the apparent FWHM in the bottom pane has no radial dependence.

Chiang & Fung (2017) suggest that the features are composed of sub-micron-sized grains which do not emit efficiently in the millimeter.

### 3.1. $^{18}\text{CO}$ Content

There is no evidence that the AU Mic system harbors a significant reservoir of molecular gas. We set a  $3\sigma$  upper limit of  $0.07 \text{ Jy km s}^{-1}$  on the CO  $J = 2 - 1$  integrated flux, obtained by integrating the flux in an  $8'' \times 8''$  box around the star between  $V_{LSRK}$  velocities of  $-10$  and  $10 \text{ km s}^{-1}$ . For a given excitation temperature, an upper limit on the total gas mass can be inferred from the upper limit on integrated flux. Assuming local thermal equilibrium (LTE) and that the gas is cospatial with the dust disk, we find the upper limit on the total gas mass to range between  $1.79 \times 10^{-7} M_{\oplus}$  and  $9.06 \times 10^{-7} M_{\oplus}$  for excitation temperatures between 10 K and 250 K.

## 4. ANALYSIS

Previous studies of the scale height of debris disks have demonstrated a degeneracy between vertical structure, radial structure, and viewing geometry (e.g., Milli et al. 2014). For example, it can be difficult to distinguish a disk that is vertically thin but slightly inclined from one that is vertically broad but perfectly edge-on. In light of this, we adopt a modeling approach that combines a simple ray-tracing code to properly project the radial and vertical flux distribution of the optically thin emission onto the sky plane with an MCMC fitting algorithm that allows us to explore the degree to which these known degeneracies impact our ability to measure the vertical structure of the disk.

### 4.1. Modeling Formalism

We use the parametric structure and ray tracing disk code described in Flaherty et al. (2015), itself an adaptation of earlier work by Rosenfeld et al. (2013). Synthetic sky-projected images are generated from a given temperature and density structure and are subsequently Fourier transformed to create model visibilities that can be directly compared to the interferometric data.

We assume the disk to be azimuthally symmetric and vertically isothermal. At a given radius  $r$ , the vertical density profile is assumed to be Gaussian with a standard deviation equal to the scale height  $H(r)$ . The assumption of Gaussian vertical structure is consistent with Brown (2001), who find that the inclination distribution of Kuiper Belt Objects (KBOs) is well described by the sum of two Gaussians.

Furthermore, the author notes that a Gaussian appears to be a “natural functional form” for the distribution of inclinations in the Kuiper Belt; Monte Carlo simulations of dynamical interactions in a disk with initial inclinations of zero produce an inclination distribution that is perfectly fit by a Gaussian. The scale height is given by  $H(r) = hr$ , where the aspect ratio  $h$  is a constant. The assumption that scale height is a linear function of radius is common for debris disk models, and we cannot justify choosing a more complex model given the resolution of the data compared to the FWHM of the disk.

The dust opacity is set to  $2.3 \text{ cm}^2 \text{ g}^{-1}$  (Beckwith et al. 1990), placing the model disk in the optically thin regime for the range of dust masses explored. For an optically thin disk, the observed thermal emission is determined by both the surface density and temperature of the dust; to break the degeneracy between these two parameters, we assume that the dust grains are in blackbody equilibrium with the central star. Thus the dust temperature at a distance  $r$  from the host star is given by

$$T_{dust}(r) = \left( \frac{L_{\star}}{16\pi r^2 \sigma} \right)^{1/4} \quad (1)$$

where  $L_{\star}$  is the bolometric luminosity of the star and  $\sigma$  is the Stefan-Boltzmann constant. We assume that the radial surface density takes the form of a power law:

$$\Sigma(r) = \begin{cases} \Sigma_c r^p & r_{in} \leq r \leq r_{out} \\ 0 & \text{otherwise} \end{cases} \quad (2)$$

where  $p$  is the power law exponent, and  $r_{in}$  and  $r_{out}$  are the disk inner and outer radius.  $\Sigma_c$  normalizes the surface density structure for a given total dust mass  $M_{dust}$ :

$$\Sigma_c = \frac{M_{dust} (p + 2)}{2\pi \left[ r_{out}^{(p+2)} - r_{in}^{(p+2)} \right]}. \quad (3)$$

The observed disk PA and inclination  $i$  are free parameters. We adopt a stellar luminosity of  $0.09 L_{\odot}$  (Plavchan et al. 2009) and a distance to the star of  $9.725 \pm 0.005 \text{ pc}$  (Gaia Collaboration et al. 2018); the observed 1.3 mm stellar flux  $F_{\star}$  is left as a free parameter for each observation date. We note that the uncertainty in the stellar distance could affect the modeled disk mass and disk radial extent, while the 10% systematic flux uncertainty could affect the modeled disk mass and stellar flux. The

disk center was set by the celestial coordinates of the star, which were obtained in 2. The spatial resolution of the resulting model sky image is set to 0.3 au per pixel, chosen to be  $\sim 10\%$  of the spatial scale sampled by the longest baseline in the data. After the model image is generated by the ray tracing code, it is Fourier transformed into the visibility domain and sampled at the same spatial frequencies as the ALMA data with the MIRIAD task `uvmodel`. This allows the model to be compared directly to the visibilities in the Fourier domain, where uncertainties are better characterized than in the image domain.

We explore the parameter space of the model using the affine-invariant formulation of the MCMC algorithm described by Goodman & Weare (2010) and implemented in Python as `emcee` (Foreman-Mackey et al. 2013). MCMC routines sample parameter space such that the density of samples in a given region is proportional to the local probability density, allowing estimation of the posterior probability functions themselves. The process therefore not only identifies regions of high probability in parameter space, but also allows uncertainties and degeneracies between parameters to be determined from the correlations between the posteriors of each parameter. A log-likelihood metric  $\ln \mathcal{L} = -\chi^2/2$  is used to assess the quality of fit between the synthetic and observed visibilities.

We assume uniform priors for all parameters; the dust mass was sampled in logarithmic space, formally equivalent to assuming a log uniform prior. Bounds placed on the logarithm of the dust mass were chosen to be large enough to so as not to impose any prior assumptions. Priors placed on the stellar flux and disk inner radius, width, power law exponent, and aspect ratio ensured that these parameters were always greater than zero. The position angle was confined to the range  $1^\circ < \text{PA} < 360^\circ$ , and the inclination to  $0^\circ < i < 90^\circ$ . Because AU Mic is so close to edge-on, the preferred inclination falls very close to the  $90^\circ$  prior upper bound. To ensure that the proximity of the solution to the edge of parameter space does not affect the posterior distribution, we investigated the effect of allowing the inclination to vary above  $90^\circ$ . Doing so produced a inclination distribution with two symmetric modes on either side of  $90^\circ$ . When the resulting unbounded inclination distribution was reparameterized such that all values fell between  $0^\circ$  and  $90^\circ$ , the original bounded inclination distribution was recovered, indicating that the placing a  $90^\circ$  prior upper bound has no effect on the inclination posterior.

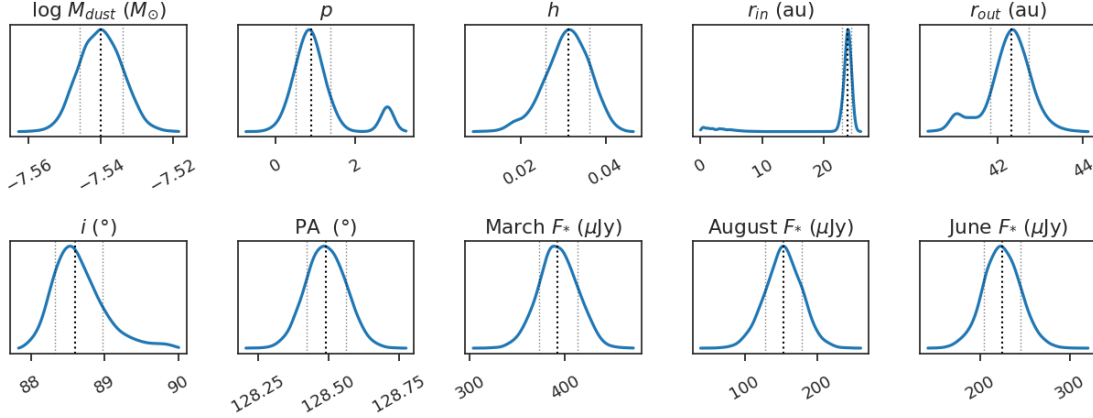


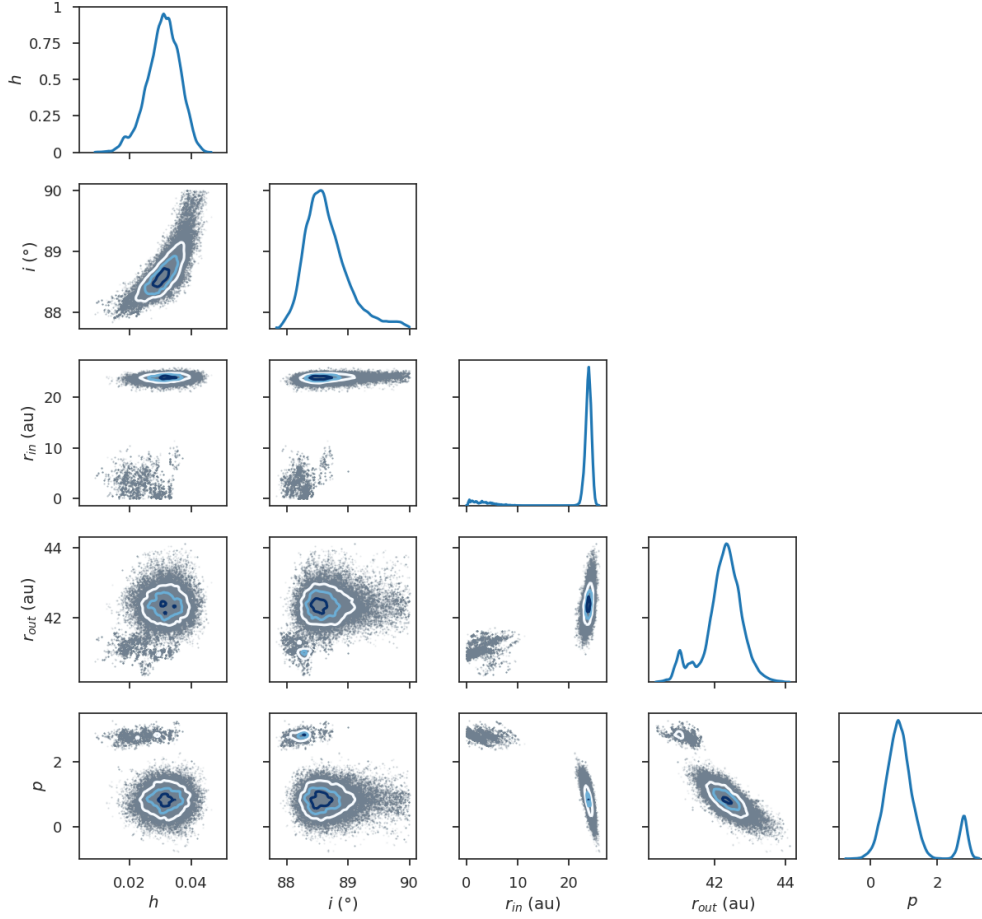
**Figure 3.** Kernel density estimates of the marginalized posterior probability distributions for the fiducial run. The central dashed line designates the median of each distribution while the outer lines mark the 16th and 84th percentiles ( $1\sigma$  confidence intervals).

We performed several MCMC runs in order to investigate a variety of model formalisms. All runs used 50 walkers, and  $10^5$  samples were drawn from each run to allow accurate statistical comparison between runs.

Initially we varied ten parameters: the logarithm of the disk dust mass ( $\log M_{\text{dust}}$ ), the disk inner radius ( $r_{\text{in}}$ ), width ( $\Delta r$ ), power law exponent ( $p$ ), scale height aspect ratio ( $h$ ), inclination ( $i$ ), position angle (PA), and finally a separate stellar flux ( $F_*$ ) for each of the three observation dates. After the fact, the posterior distribution for  $\Delta r$  was replaced by the outer radius posterior  $r_{\text{out}} = r_{\text{in}} + \Delta r$  to allow for easier interpretation. This model formalism resulted in a best-fit  $\chi^2$  value of 626163.598 (reduced  $\chi^2 = 2.053$ ), and we treat this parameterization as our fiducial model. The reduced  $\chi^2$  value indicates that our best-fit model is not a perfect fit to the data, perhaps due to the 3-sigma residuals discussed in Section 4.2. The statistical weights are likely not responsible, due to our recalculation of the weights according to the observed variance within each grid point in the  $u-v$  plane; these were checked to ensure that the distribution was indeed Gaussian.

#### 4.2. Investigating Radial Structure

Marginalized posterior probability distributions for the fiducial model parameters are shown in Figure 3. While the majority of the distributions are Gaussian, the three parameters that determine the radial structure of the disk ( $p$ ,  $r_{\text{in}}$ , and  $r_{\text{out}}$ )



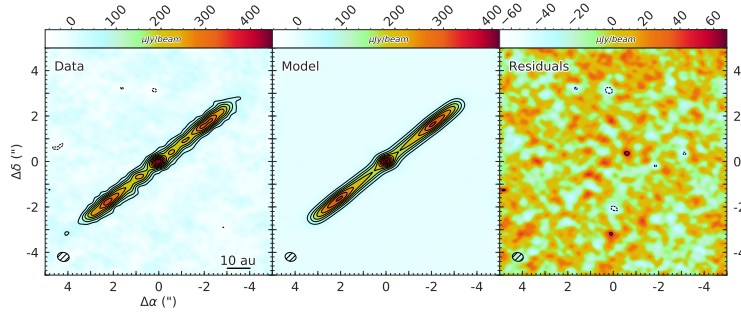
**Figure 4.** ‘Corner’ plot showing degeneracies between a subset of the free parameters for the fiducial model. Two families of solutions are visible, and are most prominent in the  $p$ ,  $r_{in}$ , and  $r_{out}$  distributions. In addition, the two-dimensional slices through parameter space show limited degeneracies between radial structure, vertical structure, and viewing geometry.

exhibit slight bimodality. All three parameters are degenerate as can be seen from the ‘corner’ plot in Figure 4; in fact, the bimodality of the three parameters is a result of the existence of two distinct families of solutions in parameter space. While the fiducial best-fit model has  $p = 0.8$ ,  $r_{in} = 24.0$  au, and  $r_{out} = 42.3$  au, a lower-likelihood family of solutions can clearly be seen in Figure 4. The highest-likelihood

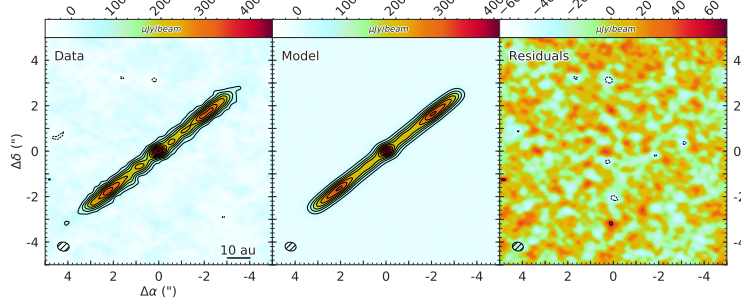
model associated with this family has  $p = 2.8$ ,  $r_{in} = 5.2$  au, and  $r_{out} = 41.0$  au. More generally, mild degeneracies between the parameters determining vertical structure, radial structure, and viewing geometry are visible, but the aspect ratio  $h$  is correlated to a significant degree only with the inclination  $i$ .

The fiducial best-fit model image and residuals found in Figure 5a provide further information as to the cause of the bimodal posterior distribution. As can be seen from the residual map, the outer regions of the disk are reproduced well by the model; however  $3\sigma$  residuals remain at the location of the star, as well as at semi-symmetric positions at a separation of  $\sim 10$  au on either side of the star. We note the semi-symmetric residuals share the locations of the local intensity maxima described in §3. The convergence of these features leads us to consider the possibility of either a dust density enhancement (a ring) or reduction (a gap) in the inner regions of the disk. As a gap/ring would cause the radial surface brightness profile of the disk to deviate from that given by the simple power law used in our modeling, it could explain the bimodality in the posterior distributions of the parameters governing disk radial structure.

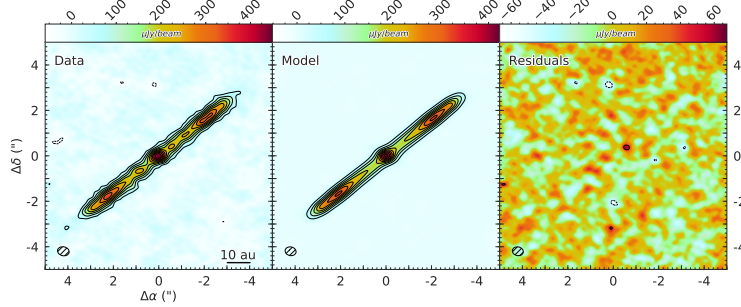
We first explored the effects of adding a gap to the inner regions of the disk. The gap inner and outer radii were left as free parameters and the dust density within the gap was set to zero. The gap consistently converged to regions where the dust density was already zero (interior to the disk inner radius or exterior to the disk outer radius); we take this as evidence that the data are not well characterized by a gap. As a next step, we experimented with adding a ring to the disk. The ring inner radius  $r_{ring}$  was once again left as a free parameter and the ring width was fixed to 0.3 au. The ring was also characterized by a dust mass  $M_{ring}$ , which was evenly distributed across the radial extent of the ring. As can be seen in Figure 5b this parameterization was better able to reproduce the ‘bump’ in the radial surface brightness profile at  $r \sim 10$  au, reducing the best-fit model residuals by  $\sim 25\%$ . However,  $2\sigma$  residuals are still present at the location of the bumps; the ring model’s failure to accurately reproduce these features could be explained by the fact that the two local intensity maxima are not perfectly symmetric about the star. Image domain analysis indicates that the bump to the SE has a separation of  $\sim 10.5$  au, while the NW bump has a separation of  $\sim 7.3$  au (Figure 2). This discrepancy could be explained if the hypothetical ring were eccentric.



(a) Fiducial run best-fit model and residuals.



(b) Ring run best-fit model and residuals.



(c) 'Skinny' disk run best-fit model and residuals.

**Figure 5.** Best-fit model image and residuals, sampled at the spatial frequencies of the ALMA data and cleaned using natural weighting. Contours are integer multiples of the ALMA data  $3\sigma$  confidence level. For the fiducial model (a),  $3\sigma$  residuals can clearly be seen at the location of the star and at semi-symmetric positions  $\sim 10$  au from the star. Adding an additional ring of dust to the model (b) reduces these residuals by  $\sim 25\%$ , but statistical analysis indicates that best-fit ring model does not conclusively describe the data better than the fiducial model. Fixing the scale height well below ALMA's resolution limits (c) results in a less statistically significant model, especially in the outer regions of the disk where ALMA is sensitive to the vertical structure of the disk.



**Table 3.** MCMC Fitting Results

Parameter	Fiducial		Disk + Ring	
	Median	Best Fit	Median	Best Fit
$\log M$ ( $M_{\odot}$ )	$-7.540^{+0.006}_{-0.006}$	-7.540	$-7.548^{+0.007}_{-0.007}$	-7.545
$p$	$0.9^{+0.5}_{-0.4}$	0.8	$0.8^{+0.6}_{-0.4}$	0.9
$h$	$0.031^{+0.005}_{-0.005}$	0.032	$0.027^{+0.004}_{-0.005}$	0.028
$r_{in}$ (au)	$23.8^{+0.6}_{-0.9}$	24.0	$24.1^{+0.6}_{-0.9}$	23.9
$r_{out}$ (au)	$42.3^{+0.4}_{-0.5}$	42.3	$42.3^{+0.4}_{-0.5}$	42.4
$i$ ( $^{\circ}$ )	$88.6^{+0.4}_{-0.3}$	88.7	$88.27^{+0.22}_{-0.16}$	88.3
PA ( $^{\circ}$ )	$128.49^{+0.07}_{-0.07}$	128.50	$128.50^{+0.07}_{-0.07}$	128.48
March $F_*$ ( $\mu\text{Jy}$ )	$390^{+20}_{-20}$	390	$370^{+20}_{-20}$	370
August $F_*$ ( $\mu\text{Jy}$ )	$150^{+20}_{-30}$	160	$150^{+20}_{-30}$	140
June $F_*$ ( $\mu\text{Jy}$ )	$220^{+20}_{-20}$	220	$220^{+20}_{-20}$	210
$r_{ring}$ (au)			$11.9^{+1.7}_{-1.8}$	10.8
$M_{ring}$ ( $M_{\oplus} \times 10^{-4}$ )			$1.8^{+0.5}_{-0.7}$	1.7
$\ln \mathcal{L}$	$-313087^{+2}_{-4}$	-313082	$-313077^{+2}_{-5}$	-313072

The median values and best-fit model parameters for the fiducial and ring parameterizations can be found in Table 3. We use both the AICc, a form of the Aikake Information Criterion (AIC) corrected for finite datasets, and the Bayesian Information Criterion (BIC) to compare goodness of fit between models with different numbers of free parameters. The best-fit ring model is preferred to the fiducial model with  $3.7\sigma$  confidence on the AICc; conversely, the fiducial model is preferred to the ring model on the BIC with  $\Delta\text{BIC} = 4.3$ . As such, we are not able to conclusively confirm the presence of an additional ring of mm dust grains in the AU Mic disk.

A model with a single  $F_*$  across all three dates was also investigated, but did not reproduce the data to the same degree of accuracy as the fiducial model. Significant residuals were visible at the location of the star, and a stellar flux varying by more than a factor of 2 over a period of months to years is preferred with  $7.3\sigma$  confidence by the AICc and with  $\Delta\text{BIC} = 36.7$ .

### 4.3. Investigating Vertical Structure

The posterior distribution for the aspect ratio  $h$  suggests that the data are capable of measuring AU Mic’s scale height despite the mild degeneracy between aspect ratio and other parameters like the radial structure and viewing geometry. Even when marginalized over these other parameters, the posterior distribution indicates a measured value of  $h = 0.031 \pm 0.005$ , which translates to a  $\sim 6\sigma$  measurement of the scale height rather than an upper limit. At the  $\sim 40$  au outer edge of the disk, this aspect ratio implies a vertical scale height of  $1.2 \pm 0.2$  au. The corresponding disk FWHM is  $2.8 \pm 0.5$  au, which is consistent with the mean image-domain FWHM of  $\sim 2.8 \pm 0.5$  au for projected separations  $\leq 30$  au in Figure 2 (due to the edge-on inclination of the disk, the outer edge of the disk sets the apparent disk thickness at all projected separations).

To verify that we in fact measured the scale height, we investigate a model parameterization in which the scale height is set to a value well below ALMA’s resolution limits. The aspect ratio is fixed at a value of 0.003, so that even at the outer edge of the disk the scale height is  $\sim 3\%$  of the beam size along the disk’s vertical axis. If the disk is in fact resolved by the observations, such a ‘skinny’ disk model should perform significantly worse than the fiducial model. Hence, we can quantify the statistical significance of our detection of the scale height by comparing the best-fit skinny model to the best-fit fiducial model. The best-fit model image and residuals are shown in Figure 5c. The skinny model results in a significantly poorer fit to the data than the fiducial model with variable aspect ratio, with the best fits differing at the  $3.9\sigma$  level according to the AICc and by a value of 7.5 on the BIC.

The preferred disk FWHM is only  $\sim 2/3$  the size of the combined-data beam projected onto the vertical axis of the disk. While it may seem improbable that we measure a scale height below the image-domain spatial resolution of the combined data, our results can be explained by the following observations. First, the beam size of the naturally weighted combined image ( $0.52'' \times 0.39''$ ) is not wholly representative of the longest baselines in the data. The smallest naturally weighted beam FWHM from the three individual observations is  $0.30''$  ( $\sim 3$  au; Table 1), while the spatial scale traced by the longest baseline is  $0.22''$  ( $\sim 2.2$  au). Second, the scale height  $H$  refers to the disk height as measured from the midplane; the observable quantity that must be resolved in order to measure the scale height is actually the total vertical thickness  $2H$ . Third, the scale height represents the standard deviation of a Gaussian

distribution of dust particles that in fact reaches well beyond the extent of the scale height. For example, considering that the peak SNR of the data is  $\sim 23$  and that the vertical distribution of dust is assumed to be Gaussian, the SNR should remain above 3 over a total vertical extent of  $\sim 0.38''$  (3.8 au). The combination of these factors indicates that it is plausible that we are able to detect a scale height smaller than the resolution of the image-domain data.

## 5. DISCUSSION

Parametric modeling suggests that AU Mic’s debris disk is nearly edge on, exhibits an increasing surface density with radius until  $\sim 42$  au, and reaches a maximum scale height of  $\sim 1.2$  au. There is also marginal evidence for an additional annulus of dust at  $r \sim 10$  au. Here we compare the results of our analysis with previous studies of AU Mic’s debris disk. Relevant quantities in the literature have been scaled by the new Gaia distance, although in most cases the scaling has no effect on the first significant figure. When scaling by the Gaia distance does change significant digits, the resulting value is referred to as “Gaia-corrected.”

### 5.1. Disk Geometry

The geometric properties of the disk inferred from our modeling agree well with the literature. Our median inclination of  $88.6^{+0.4}_{-0.3}$  is consistent with previous estimates of the disk’s inclination within uncertainties (Metchev et al. 2005; Krist et al. 2005). The median PA of  $128.49 \pm 0.07$  falls within uncertainties of measurements by MacGregor et al. (2013) and Krist et al. (2005); however, the limb-averaged PA interior to 50 au from Metchev et al. (2005) is  $129.8 \pm 0.2$ , and Schneider et al. (2014) report an optical-wavelength PA of  $127.8 \pm 0.2$  between 50 au to 100 au.

### 5.2. Dust Mass

The preferred dust mass ( $0.01 M_{\oplus}$  assuming an opacity of  $2.3 \text{ cm}^2 \text{ g}^{-1}$ ) is identical to the value derived by MacGregor et al. (2013) from a 1.3 mm disk flux density of  $7.14^{+0.12}_{-0.25} \text{ mJy}$  and an opacity of  $2.7 \text{ cm}^2 \text{ g}^{-1}$ . Matthews et al. (2015) also report a mass of  $0.01 M_{\oplus}$  with 20% uncertainty from a  $850 \mu\text{m}$  disk flux density of  $12.5 \pm 1.5 \text{ mJy}$  and an opacity of  $1.7 \text{ cm}^2 \text{ g}^{-1}$ . Liu et al. (2004) also take the opacity to be  $1.7 \text{ cm}^2 \text{ g}^{-1}$ , and report  $0.011 M_{\oplus}$  from a disk flux density of  $14.4 \pm 1.8 \text{ mJy}$  at  $850 \mu\text{m}$ . Finally, Strubbe & Chiang (2006) calculate  $0.01 M_{\oplus}$  by deriving a steady-state collisional cascade grain size distribution and fitting the disk’s surface brightness and thermal spectrum to *V*- and *H*-band HST observations.

### 5.3. *Gas Mass*

As discussed in §3, even a large gas excitation temperature of 250 K implies a  $3\sigma$  upper limit on the  $^{12}\text{CO}$  mass of only  $9.06 \times 10^{-7} M_{\oplus}$ ; combined with our preferred dust mass, this mass corresponds to an upper limit on the gas-to-dust ratio of  $\sim 10^{-4}$ . Such a low dust-to-gas ratio excludes the possibility of gas influencing the millimeter grain kinematics, and thus our measurement of the scale height.

### 5.4. *Stellar Activity*

Our analysis indicates with high confidence that AU Mic exhibited long-term millimeter variability over the  $\sim 1.5$  yr observation period. The stellar fluxes preferred by our modeling vary by more than a factor of two from one observation to the next, and are comparable to the best-fit flux of  $320 \pm 60 \mu\text{Jy}$  from MacGregor et al. (2013). It seems likely that this variability is distinct from the 6 minute flare spanning two orders of magnitude that occurred during the June observations. That being said, we cannot rule out the possibility that the observations caught the star in varying states of flare decay, especially as White (1996) note that shorter-wavelength radio flares tend to have slower decay timescales. Simulations of radio emission from low-mass stars allow for variability of more than a factor of two over the entire longitudinal extent of a star (Llama et al. 2018); it is also possible that different longitudinal regions of AU Mic were facing Earth during the three observations. Cox & Gibson (1985) detect small-scale ( $\sim 50\%$ ) variations over a two-week period in 2 cm to 20 cm observations of AU Mic with the VLA, possibly due to ‘several independent mini-flares’ or rotational modulation of the star. In fact, factor of  $\sim 2$  variability over months to years is typical of ‘quiescent’ microwave emission from cool stars (Guedel 1994). Regardless of the origin of AU Mic’s short- and long-term variability, we emphasize the importance of accounting for stellar emission/variability in observations of circumstellar disks around low-mass stars, especially in light of the Proxima Centauri flare discovered by MacGregor et al. (2018).

### 5.5. *Radial Structure*

Modeling of the radial structure discussed in §4.2 is broadly consistent with the previous analysis of millimeter wavelength emission from the disk performed by MacGregor et al. (2013) as can be seen in Figure 6. However, the factor of  $\sim 2$  increase in spatial resolution introduces additional interpretive complexities when comparing the results. While our outer radius is only 2 au larger than the previously re-

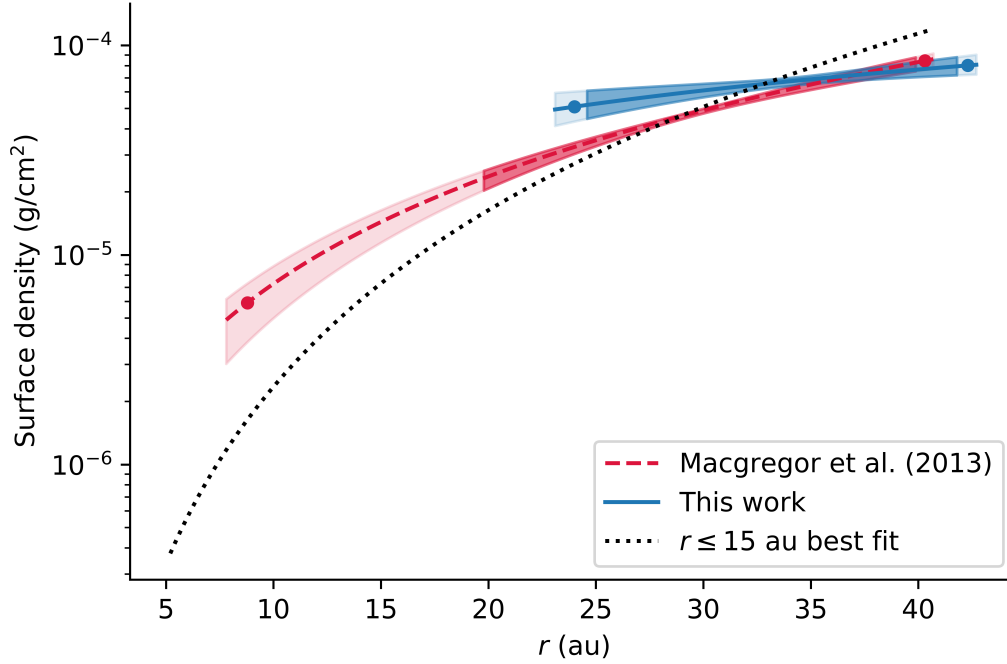


**Figure 6.** Comparison between the best-fit surface density profiles obtained in [MacGregor et al. \(2013\)](#) (dashed red line) and this work (solid blue line). Also included is the best-fit surface density profile associated with the lower-likelihood family of solutions (dotted black line). The vertical extent of the shaded regions marks  $1\sigma$  confidence intervals on the surface density. The points designate the best-fit inner and outer radii for each model, and the horizontal extent of the more transparent shaded regions show  $1\sigma$  confidence intervals on the inner and outer radii. Not included in the uncertainties are the 10% flux uncertainties of each observation.

ported Gaia-corrected value of 40.3 au (confidence intervals are  $\sim 0.4$  au for both measurements), things become more complicated when considering the inner radius  $r_{in}$  and surface brightness power law index  $p$ . In contrast to  $r_{in} = 23.8^{+0.6}_{-0.9}$  au preferred by our MCMC analysis, [MacGregor et al. \(2013\)](#) report a Gaia-corrected  $r_{in} = 8.5^{+11.0}_{-1.0}$  au. Neither value of the inner radius is well constrained: the authors report a Gaia-corrected  $3\sigma$  upper limit of 20 au, whereas conversely we find a  $2\sigma$  lower limit of  $\sim 1$  au. Similar discrepancies arise in the posterior distribution for  $p$ , which is degenerate with  $r_{in}$ . While [MacGregor et al. \(2013\)](#) finds  $p = 2.32^{+0.21}_{-0.31}$ , we recover a median value of  $p = 0.9^{+0.5}_{-0.4}$ . In our analysis, the uncertainties in

these two parameters arise from the existence of two families of solutions: one at  $r_{in} \sim 23$  au,  $r_{out} \sim 42$  au,  $p \sim 0.8$  and another at  $r_{in} \sim 5$  au,  $r_{out} \sim 41$  au,  $p \sim 2.8$  (Figure 6). The latter family, which has a lower likelihood, is probably associated with the local intensity maxima on either of the star examined in §4. Our exploratory modeling of these features raises the possibility of an annulus of dust interior to the main disk—if such an annulus does exist, the  $\sim 2$  times lower resolution observations from MacGregor et al. (2013) would probably not have been able to distinguish the annulus emission from that of the main disk. In fact, an unresolved annulus would likely bias the inner radius preferred by the authors’ modeling towards smaller values and could account for the differences in our characterization of the radial structure.

While the annulus model provides only a marginally significantly improved fit to the data, previous observations spanning a wide range of wavelengths have recovered surface brightness enhancements at the same projected stellocentric separation ( $\sim 10$  au) as the hypothetical annulus. A local maximum is present to the SE of the star at this separation in lower-resolution ALMA observations by MacGregor et al. (2013), and there is a suggestive peak in the noise on the opposite side of the star as well. Although these surface brightness enhancements do not attain  $3\sigma$  significance after subtraction of an axisymmetric model, the independent detection of these features in both data sets suggests that they may be real. Schneider et al. (2014) also observe an optical-wavelength ‘bump’  $\sim 13$  au SE of the star and slightly elevated from the disk midplane (i.e. to the NE). No matching surface brightness enhancement is observed on the NW side of the disk, which is obscured by the STIS occulting wedge for  $r \lesssim 12$  au. On the other hand, the scattered light emission on the NW side is not symmetric about the midplane and the authors tentatively identify a warp below the midplane extending to a distance of  $\sim 45$  au from the star. They note that these features may share a common cause, and posit that dust orbits in the inner disk are non-coplanar with those found at larger separations.

Near-infrared GPI observations presented in Wang et al. (2015) further corroborate the presence of a ‘bump’ to the SE, characterized by a FWHM roughly triple the FWHM at an equivalent separation on the NW side of the disk. No features are detected at a corresponding separation to the NW. Figure 4 of Wang et al. (2015) shows a composite map of the bump as seen by GPI, STIS, and ALMA; the common location of the bump in both scattered light and mm observations would indicate that the mm- and micron-sized grains are cospatial. The micron-sized grains traced by

scattered light, and all larger bodies ranging up to the cm-to-m sizes characterizing the top of the collisional cascade, are thought to originate from a narrow ‘birth ring’ at  $\sim 40$  au (Strubbe & Chiang 2006). Thus it is possible that the millimeter bump visible in this work and in MacGregor et al. (2013) are actually cospatial with the scattered light bump and that all features are located at a true stellocentric separation of  $\sim 40$  au (the apparent stellocentric separation of  $\sim 10$  au would be due to projection). In principle, the true stellocentric separation could be constrained by the range of temperatures allowed by AU Mic’s SED. However such an analysis would be subject to assumptions about the grain size distribution and is beyond the scope of this vertical structure-oriented work.

### 5.6. Vertical Structure

As discussed in §4.3, our MCMC analysis yields a median aspect ratio of  $h = 0.031 \pm 0.005$ ; at a reference point of 40 au, this translates to a vertical scale height  $H = 1.2 \pm 0.2$  au. This measurement is marginally consistent with values cited in the literature, ranging from roughly 0.6 au to 2 au and derived from observations spanning the optical to the sub-millimeter. Schüppler et al. (2015) place an upper limit of 0.05 rad on the 1.3 mm opening angle (equivalent to the aspect ratio for small angles) by extracting the image-domain vertical profile from vertically unresolved ALMA observations presented in MacGregor et al. (2013), and estimate a visible-wavelength opening angle of 0.03 rad by reading off the vertical scale height from STIS observations of the disk in Schneider et al. (2014). Metchev et al. (2005) approximate a  $H$ -band Keck FWHM of  $\sim 4$  au at a separation of 40 au; Krist et al. (2005) fit a vertical Lorentzian profile to multicolor HST observations of the disk and find the FWHM interior to 50 au to fall between 2.5 au and 3.5 au.

Because the measurements quoted above are determined from the observed vertical thickness of AU Mic’s disk, they can be affected by the radial structure and viewing geometry of the disk as well as scattering effects. As such, parametric modeling provides a more reliable way to assess AU Mic’s vertical structure. Krist et al. (2005) report a FWHM between 1.73 au and 1.74 au at a separation of 20 au from three-dimensional scattering models. Collisional modeling can also be used to learn about AU Mic’s vertical structure: collisional velocities—and thus dust production—are affected by the maximum eccentricity  $e_{max}$  of planetesimal orbits, which in turn can be related to the disk vertical structure (see §5.7 below). Schüppler et al. (2015) perform such modeling constrained by photometric observations spanning visible to

millimeter wavelengths and quote a reference model opening angle of 0.015 rad. The authors go on to note that an opening angle of 0.005 rad better reproduces the disk spectral energy distribution (SED) in the long-wavelength regime beyond  $100\ \mu\text{m}$ , but is unable to reproduce flux measurements for  $\lambda \leq 70\ \mu\text{m}$ .

In sum, estimates of AU Mic’s vertical structure vary depending on the wavelength of observation, the techniques used, and the assumptions made. Rigorous comparison between measurements in the literature is difficult—for example, [Krist et al. \(2005\)](#) assume a flared vertical profile while other authors use a linear parameterization for the scale height. Nevertheless, some general statements may be made. Values determined from optical and near-infrared observations range from roughly  $H = 1.2\text{ au}$  to  $2\text{ au}$  at a radius of  $40\text{ au}$ , while the values determined at least in part from mm observations range from  $H = 0.6\text{ au}$  to  $2\text{ au}$ , the latter being an upper limit. Estimates based on millimeter observations (including this work) tend to be smaller than those derived from shorter-wavelength observations, although the two wavelength regimes do not provide radically different values.

It is not unexpected that optical and infrared measurements of the scale height would exceed millimeter-wavelength estimates. [Thébault \(2009\)](#) suggests that the smaller grains traced by short-wavelength observations can be placed on inclined orbits by radiation pressure (and to first order, disk winds) even in the absence of large bodies dynamically stirring the disk. This effect preferentially excites smaller dust grains, ‘puffing’ up the disk at mid-IR to visible wavelengths, while the larger grains that dominate emission at longer wavelengths remain near the midplane. [Thébault \(2009\)](#) proposes a ‘natural’ minimum debris disk thickness due to stellar winds and radiation pressure of  $h = 0.04 \pm 0.02$  as seen at wavelengths smaller than  $50\ \mu\text{m}$ . The author also runs a collisional model tailored to the AU Mic system assuming no intrinsic dynamical excitation, and reports  $H = 1\text{ au}$  for  $r \leq 40\text{ au}$  when degraded to the resolution of scattered light images. Although this scale height falls within the range of ‘natural’ debris disk thicknesses, the author stresses that this does not amount to an assertion that the disk is dynamically cold due to the simplicity of their model and fitting process.

In recent years, the vertical structure of several other debris disks has been tentatively resolved with ALMA.  $\sim 5.5\text{ au}$  spatial resolution observations of CO  $J = 3 - 2$  and  $2 - 1$  line emission from the edge-on  $\beta$  Pic debris disk presented by [Matrà et al. \(2017\)](#) suggest that the disk is resolved in the vertical direction. The beam-subtracted



apparent FWHM, determined in a similar manner as the bottom pane of Figure 2 in this work, ranges between  $\sim 7$  au and 12 au over the  $\sim 100$  au radial extent of the disk. Assuming an Keplerian rotation and edge-on inclination, the authors report the following scale height-radius relation:

$$H = 7.0 \pm 0.6 \times \left( \frac{R}{85 \text{ au}} \right)^{0.75 \pm 0.02} \text{ au} \quad (4)$$

where the scale height  $H$  is the standard deviation of the Gaussian vertical density distribution. For reference to our work, this corresponds to a scale height of 4 au at a separation of 40 au. Kennedy et al. (2018) analyze  $11.6 \text{ au} \times 13.1 \text{ au}$  spatial resolution observations of the HR 4796A debris disk, reporting a marginal detection of the disk scale height. The authors find that a vertically resolved ring ( $\text{FWHM} = 7 \pm 1 \text{ au}$ ) is favored over a vertically unresolved ring ( $\text{FWHM} < 4 \text{ au}$ ) with  $\Delta BIC = 6.8$ . This FWHM corresponds to a Gaussian standard deviation  $H \approx 3.0 \pm 0.4 \text{ au}$  and, at the  $\sim 80 \text{ au}$  radial location of the ring, a scale factor of  $h \approx 0.038 \pm 0.005$ . Although the relative  $BIC$  reported by the authors meets the condition for ‘strong’ evidence of a statistically higher-quality fit ( $\Delta BIC > 6$ ), the fact that the preferred FWHM is nearly a factor of two smaller than the spatial resolution of the data calls into question the certainty of the measurement. In sum, the vertical structure of debris disks is just beginning to be resolved in the millimeter thanks to the improvements in sensitivity and resolution provided by ALMA; to our knowledge, AU Mic exhibits the narrowest millimeter-wavelength scale height of any known debris disk.

### 5.7. Inferring the Mass of Stirring Bodies

Information regarding the bodies dynamically stirring AU Mic’s disk can be recovered by relating the scale height to the dynamical excitation of the disk’s dust grains. As discussed by Thébault (2009) and Quillen et al. (2007), the planetesimals responsible for stirring the disk impart kinetic energy to the dust, perturbing them from a Keplerian orbit and thus increasing their orbital eccentricity dispersion  $\langle e^2 \rangle$ . Here we define  $\bar{e} = \sqrt{\langle e^2 \rangle}$  and  $\bar{i} = \sqrt{\langle i^2 \rangle}$ , where  $\langle i^2 \rangle$  is the inclination dispersion of the dust grain orbits. In equilibrium there is an equipartition between the vertical and in-plane components of the velocities imparted to the grains, so  $\bar{i} = \bar{e}/2$ . For low inclinations, inclination can be related to the observed aspect ratio using  $\bar{i} = \sqrt{2}h$ . The interparticle relative velocity  $\langle v_{rel} \rangle$  can then be determined directly from observables using the following relation (Wetherill & Stewart 1993; Wyatt &

Dent 2002):

$$\langle v_{rel} \rangle = v_{Kep}(r) \sqrt{i^2 + 1.25e^2} = v_{Kep}(r) \sqrt{12}h \quad (5)$$

where  $v_{Kep}(r)$  is the Keplerian velocity at radius  $r$ . Adopting a stellar mass of  $0.5 M_{\odot}$  from the literature (Plavchan et al. 2009; Houdebine & Doyle 1994) and taking  $r = 40$  au,  $h = 0.031 \pm 0.005$  yields  $v_{rel} = 360 \pm 60$  m/s.

The velocity dispersion of the dust grains will be excited to about the escape velocity of the largest bodies governing the disk dynamics in the absence of any significant damping of their velocity dispersion. This result arises because viscous stirring has a larger cross section (i.e. shorter characteristic timescale) than collisions as long as the velocity dispersion is less than the escape velocity of the largest bodies that dominate the stirring. The two cross sections (and timescales) become comparable as  $v_{rel}$  approaches  $v_{esc}$  and collisions start to dominate, limiting the growth of  $v_{rel}$  to about  $v_{esc}$  (Schlichting 2014, e.g.). As such, we can use our estimate for  $v_{rel}$  to place a lower limit on the escape velocity and thus size  $a_{big}$  of bodies stirring the disk. Assuming a density of  $2 \text{ g cm}^{-3}$ , we find  $a_{big} \sim 340 \pm 60$  km and  $m_{big} \sim 3.2 \pm 1.1 \times 10^{20}$  kg, i.e. 2.5% the mass of Pluto.

On the other hand, the disk may be in a steady state in which velocity damping is balanced with excitation (rather than damping being inefficient). Under this condition the scale height provides an estimate of the total mass of stirring bodies, not their size. To relate the observed disk scale height to the total mass of bodies stirring the disk, we refer to theoretical models of steady state size-dependent velocity distributions in the collisional cascade described in Pan & Schlichting (2012). Assuming a scale height of 1.2 au at 40 au, a stellar mass of  $0.5 M_{\odot}$ , and a dust mass of  $0.01 M_{\oplus}$ , these models indicate a total dynamical mass of  $\sim 1.5 M_{\oplus}$ . If all of the  $1.5 M_{\oplus}$  were locked up in a single body, it would have a radius of  $\sim 1.1 R_{\oplus}$  assuming a mean density of  $5.5 \text{ g cm}^{-3}$  characteristic of Earth.

In sum, the largest bodies in the AU Mic disk cannot be smaller than  $340 \pm 60$  km or they would not be able to stir the dust grains to the velocity dispersion inferred from the measured scale height. Conversely, the largest body stirring the disk cannot be larger than  $\sim 1.5 M_{\oplus}$  or the scale height would exceed the value measured in this work. It should also be noted that because the scale height measured at the outer edge of the disk is comparable to the spatial resolution of the data, and since scale height decreases with decreasing radius, the observations are only sensitive to the

scale height near the  $\sim 40$  au outer disk radius. If the disk is stirred by an ensemble of 340 km planetesimals, they would necessarily be located within this outer region of the disk. That being said, a planet is capable of stirring a dynamically cold disk at a distance of roughly five Hill Radii (Greenzweig & Lissauer 1990), defined as

$$r_H = r \left( \frac{m_p}{3M_\star} \right)^{1/3} \quad (6)$$

where  $r$  and  $m_p$  are the orbital separation and mass of the perturber and  $M_\star$  is the stellar mass. Thus if the mass were concentrated within a single  $1.5 M_\oplus$  body, it could be located as far as 3 au interior or exterior to the debris belt. Similarly, our measurement of the scale height excludes Uranus or Neptune analogs of mass  $\sim 15 M_\oplus$  within 6 au of the parent body belt.

The properties of the perturbers estimated in this work are consistent with those inferred by Chiang & Fung (2017) on independent grounds using the time-variable infrared observations by Boccaletti et al. (2015, 2018). Our lower limit on the perturbing body size of  $\sim 340$  km fits with the  $\sim 400$  km radius for their Varuna-like progenitor (for reference, Varuna is among the larger objects in the Kuiper belt). Moreover, there should be on the order of  $10^3$  such objects according to their scenario (the argument is as follows: since the lifetime of the debris left from the catastrophic disruption of a Varuna-sized progenitor is  $\sim 3 \times 10^4$  yr (Chiang & Fung 2017, their equation 21), and since the age of the AU Mic system is  $\sim 20$  Myr, there must have been  $20 \text{ Myr} / 3 \times 10^4 \text{ yr} \sim 700$  such progenitors over the system lifetime. A population on the order of  $10^3$  bodies then yields an order-unity probability for observing the aftermath of a single catastrophic collision today). An ensemble of  $\sim 10^3$  bodies each with a mass of  $4\pi/3 \cdot 2.5 \text{ g cm}^{-3} \cdot (400 \text{ km})^3 \sim 1 \times 10^{-3} M_\oplus$  amounts to a total mass of  $\sim 0.1 M_\oplus$ , safely below the upper limit of  $1.5 M_\oplus$  established by our present work.

## 6. CONCLUSION

We have presented new 1.3 mm ALMA observations of thermal dust emission from the debris disk around AU Mic at nearly double the angular resolution of previous observations. Both the vertical and radial structure of the disk are resolved. MCMC analysis prefers an aspect ratio  $h = 0.031$ , corresponding to a vertical scale height  $H = 1.2$  au in the outer regions of the disk. Our analysis suggests that this

is not an upper limit; a model with vertically resolved structure provides a statistically improved fit to the data over a model with unresolved vertical structure at a  $4\sigma$  confidence level. Furthermore, the disk vertical FWHM derived from parametric modeling corresponds well with image-domain estimates of the beam-subtracted FWHM of the emission perpendicular to the disk plane.

By comparing our measurement of the scale height to the steady-state collisional modeling of [Pan & Schlichting \(2012\)](#) we are able to place constraints on the mass and size of bodies stirring AU Mic’s disk. In the lower-limit case where collisional velocity damping is inefficient, the stirring bodies would have a radius of  $340 \pm 60$  km, corresponding to a characteristic mass  $\sim 50$  times less than that of Pluto. On the other hand, velocity damping may balance stirring; this condition allows us to place an upper limit of  $\sim 1.5 M_{\oplus}$  on the mass of stirring bodies. This is a dynamical mass, distinct from the lunar mass of dust grains inferred from the millimeter flux of the disk. These results therefore rule out the presence of a gas giant or Neptune analog in the outer disk, but are suggestive of a significant population of large asteroids having a combined mass of less than one Earth. Such a population has been inferred on independent grounds using time-variable infrared observations ([Chiang & Fung 2017](#)).

We see no indication of the fast-moving features detected by [Boccaletti et al. \(2015\)](#), but the data are suggestive of an additional ring of dust at  $\sim 10$  au. Models with a ring interior to the main disk provide a better fit to the data, but measures of statistical significance remain equivocal as to whether such models minimize the information lost in the modeling process. Thus the presence of a ring remains uncertain. P. Plavchan et al. (in preparation) propose a Jovian-mass exoplanet candidate interior to 1 au, but AU Mic’s stellar activity make it difficult to confirm the radial velocity detection.

Looking forward, the scale height measurement presented in this work could be combined with other measurements of AU Mic’s scale height at widely-separated (sub)millimeter wavelengths. This would allow the size-dependent velocity dispersion and internal strengths of bodies in AU Mic’s collisional cascade to be constrained, testing the assumption of collisional cascade theory that velocity dispersion is constant with grain size. The  $450 \mu\text{m}$  ALMA Band 9 observations of AU Mic presented in the forthcoming work of Carter et al. (in preparation) may be able to provide such constraints. Our measurements of the AU Mic system provide a proof of concept that

spatially resolved observations of the vertical structure at millimeter wavelengths can constrain the presence of Uranus and Neptune analogs and even large Kuiper belt object analogues, which are undetectable by standard planet-detection techniques. Applying this technique to other high-inclination debris disks with a range of central stellar masses will provide unique constraints on the prevalence of large perturbing bodies throughout the Galaxy.

## ACKNOWLEDGEMENTS

C.D. is sponsored by a NASA CT Space Grant Undergraduate Research Fellowship and Wesleyan University’s Research in the Sciences Fellowship. C.D., A.M.H., E.C., and K.F. gratefully acknowledge support from NSF grant AST-1412647. E.I.C. acknowledges support from the National Science Foundation. H.E.S gratefully acknowledges support from NASA grant NNX15AK23G. J.M.C. acknowledges support from the National Aeronautics and Space Administration under grant No. 15XRP15\_20140 issued through the Exoplanets Research Program. M.P. gratefully acknowledges support from NASA grants NNX15AM35G and NNX15AK23G. This paper makes use of the following ALMA data: ADS/JAO.ALMA#2012.1.00198.S. ALMA is a partnership of ESO (representing its member states), NSF (USA) and NINS (Japan), together with NRC (Canada), MOST and ASIAA (Taiwan), and KASI (Republic of Korea), in cooperation with the Republic of Chile. The Joint ALMA Observatory is operated by ESO, AUI/NRAO and NAOJ. The National Radio Astronomy Observatory is a facility of the National Science Foundation operated under cooperative agreement by Associated Universities, Inc. This work has made use of data from the European Space Agency (ESA) mission *Gaia* (<https://www.cosmos.esa.int/gaia>), processed by the *Gaia* Data Processing and Analysis Consortium (DPAC, <https://www.cosmos.esa.int/web/gaia/dpac/consortium>). Funding for the DPAC has been provided by national institutions, in particular the institutions participating in the *Gaia* Multilateral Agreement.

*Software:* CASA (McMullin et al. 2007), MIRIAD (Sault et al. 1995), NumPy (Van Der Walt et al. 2011), Astropy (The Astropy Collaboration et al. 2018), Pandas (McKinney 2010), emcee (Foreman-Mackey et al. 2013), Uncertainties, <http://pythonhosted.org/uncertainties/>

## REFERENCES

- Artymowicz, P. 1997, Annual Review of Earth and Planetary Sciences, 25, 175, doi: [10.1146/annurev.earth.25.1.175](https://doi.org/10.1146/annurev.earth.25.1.175)
- Augereau, J.-C., & Beust, H. 2006, A&A, 455, 987, doi: [10.1051/0004-6361:20054250](https://doi.org/10.1051/0004-6361:20054250)
- Beckwith, S. V. W., Sargent, A. I., Chini, R. S., & Gusten, R. 1990, AJ, 99, 924, doi: [10.1086/115385](https://doi.org/10.1086/115385)
- Binks, A. S., & Jeffries, R. D. 2014, MNRAS, 438, L11, doi: [10.1093/mnrasl/slt141](https://doi.org/10.1093/mnrasl/slt141)
- Boccaletti, A., Thalmann, C., Lagrange, A.-M., et al. 2015, Nature, 526, 230, doi: [10.1038/nature15705](https://doi.org/10.1038/nature15705)
- Boccaletti, A., Sezestre, E., Lagrange, A. M., et al. 2018, ArXiv e-prints, arXiv:1803.05354. <https://arxiv.org/abs/1803.05354>
- Brown, M. E. 2001, AJ, 121, 2804, doi: [10.1086/320391](https://doi.org/10.1086/320391)
- Chiang, E., & Fung, J. 2017, ApJ, 848, 4, doi: [10.3847/1538-4357/aa89e6](https://doi.org/10.3847/1538-4357/aa89e6)
- Cox, J. J., & Gibson, D. M. 1985, in IN: Radio stars; Proceedings of the Workshop on Stellar Continuum Radio Astronomy, Boulder, CO, August 8-10, 1984 (A86-38003 17-90). Dordrecht, D. Reidel Publishing Co., 1985, p. 233-236., Vol. 116, 233–236
- Cranmer, S. R., Wilner, D. J., & MacGregor, M. A. 2013, ApJ, 772, 149, doi: [10.1088/0004-637X/772/2/149](https://doi.org/10.1088/0004-637X/772/2/149)
- Ercolano, B., & Pascucci, I. 2017, Royal Society Open Science, 4, 170114, doi: [10.1098/rsos.170114](https://doi.org/10.1098/rsos.170114)
- Flaherty, K. M., Hughes, A. M., Rosenfeld, K. A., et al. 2015, ApJ, 813, 99, doi: [10.1088/0004-637X/813/2/99](https://doi.org/10.1088/0004-637X/813/2/99)
- Flaherty, K. M., Hughes, A. M., Rose, S. C., et al. 2017, ApJ, 843, 150, doi: [10.3847/1538-4357/aa79f9](https://doi.org/10.3847/1538-4357/aa79f9)
- Foreman-Mackey, D., Hogg, D. W., Lang, D., & Goodman, J. 2013, PASP, 125, 306, doi: [10.1086/670067](https://doi.org/10.1086/670067)
- Gaia Collaboration, Brown, A. G. A., Vallenari, A., et al. 2018, ArXiv e-prints, arXiv:1804.09365. <https://arxiv.org/abs/1804.09365>
- Gaia Collaboration, Prusti, T., de Bruijne, J. H. J., et al. 2016, A&A, 595, A1, doi: [10.1051/0004-6361/201629272](https://doi.org/10.1051/0004-6361/201629272)
- Goodman, J., & Weare, J. 2010, Communications in Applied Mathematics and Computational Science, Vol. 5, No. 1, p. 65-80, 2010, 5, 65, doi: [10.2140/camcos.2010.5.65](https://doi.org/10.2140/camcos.2010.5.65)
- Greenzweig, Y., & Lissauer, J. J. 1990, Icarus, 87, 40, doi: [10.1016/0019-1035\(90\)90021-Z](https://doi.org/10.1016/0019-1035(90)90021-Z)
- Guedel, M. 1994, The Astrophysical Journal Supplement Series, 90, 743, doi: [10.1086/191899](https://doi.org/10.1086/191899)
- Houdebine, E. R., & Doyle, J. G. 1994, A&A, 289, 185
- Hughes, A. M., Duchene, G., & Matthews, B. 2018, ArXiv e-prints. <https://arxiv.org/abs/1802.04313>
- Kalas, P., Liu, M. C., & Matthews, B. C. 2004, Science, 303, 1990, doi: [10.1126/science.1093420](https://doi.org/10.1126/science.1093420)
- Kennedy, G. M., Marino, S., Matrà, L., et al. 2018, MNRAS, 475, 4924, doi: [10.1093/mnras/sty135](https://doi.org/10.1093/mnras/sty135)
- Krist, J. E., Ardila, D. R., Golimowski, D. A., et al. 2005, AJ, 129, 1008, doi: [10.1086/426755](https://doi.org/10.1086/426755)

- Liu, M. C., Matthews, B. C., Williams, J. P., & Kalas, P. G. 2004, *ApJ*, 608, 526, doi: [10.1086/392531](https://doi.org/10.1086/392531)
- Llama, J., Jardine, M. M., Wood, K., Hallinan, G., & Morin, J. 2018, *ApJ*, 854, 7, doi: [10.3847/1538-4357/aaa59f](https://doi.org/10.3847/1538-4357/aaa59f)
- MacGregor, M. A., Weinberger, A. J., Wilner, D. J., Kowalski, A. F., & Cranmer, S. R. 2018, *ApJ*, 855, doi: [10.3847/2041-8213/aaad6b](https://doi.org/10.3847/2041-8213/aaad6b)
- MacGregor, M. A., Wilner, D. J., Rosenfeld, K. A., et al. 2013, *ApJL*, 762, L21, doi: [10.1088/2041-8205/762/2/L21](https://doi.org/10.1088/2041-8205/762/2/L21)
- Malo, L., Doyon, R., Feiden, G. A., et al. 2014, *ApJ*, 792, 37, doi: [10.1088/0004-637X/792/1/37](https://doi.org/10.1088/0004-637X/792/1/37)
- Mamajek, E. E., & Bell, C. P. M. 2014, *MNRAS*, 445, 2169, doi: [10.1093/mnras/stu1894](https://doi.org/10.1093/mnras/stu1894)
- Matrà, L., Dent, W. R. F., Wyatt, M. C., et al. 2017, *MNRAS*, 464, 1415, doi: [10.1093/mnras/stw2415](https://doi.org/10.1093/mnras/stw2415)
- Matthews, B. C., Kennedy, G., Sibthorpe, B., et al. 2015, *ApJ*, 811, 100, doi: [10.1088/0004-637X/811/2/100](https://doi.org/10.1088/0004-637X/811/2/100)
- McKinney, W. 2010, in *Proceedings of the 9th Python in Science Conference*, ed. S. van der Walt & J. Millman, 51 – 56
- McMullin, J. P., Waters, B., Schiebel, D., Young, W., & Golap, K. 2007, in *Astronomical Data Analysis Software and Systems XVI ASP Conference Series*, Vol. 376, proceedings of the conference held 15-18 October 2006 in Tucson, Arizona, USA. Edited by Richard A. Shaw, Frank Hill and David J. Bell., p.127, Vol. 376, 127
- Metchev, S. A., Eisner, J. A., Hillenbrand, L. A., & Wolf, S. 2005, *ApJ*, 622, 451, doi: [10.1086/427869](https://doi.org/10.1086/427869)
- Milli, J., Lagrange, A.-M., Mawet, D., et al. 2014, *A&A*, 566, A91, doi: [10.1051/0004-6361/201323130](https://doi.org/10.1051/0004-6361/201323130)
- Montesinos, B., Eiroa, C., Krivov, A. V., et al. 2016, *A&A*, 593, A51, doi: [10.1051/0004-6361/201628329](https://doi.org/10.1051/0004-6361/201628329)
- Moshir et al. 1990, in *IRAS Faint Source Catalogue*, version 2.0 (1990)
- Pan, M., & Schlichting, H. E. 2012, *ApJ*, 747, 113, doi: [10.1088/0004-637X/747/2/113](https://doi.org/10.1088/0004-637X/747/2/113)
- Plavchan, P., Werner, M. W., Chen, C. H., et al. 2009, *ApJ*, 698, 1068, doi: [10.1088/0004-637X/698/2/1068](https://doi.org/10.1088/0004-637X/698/2/1068)
- Quillen, A. C., Morbidelli, A., & Moore, A. 2007, *MNRAS*, 380, 1642, doi: [10.1111/j.1365-2966.2007.12217.x](https://doi.org/10.1111/j.1365-2966.2007.12217.x)
- Rosenfeld, K. A., Andrews, S. M., Hughes, A. M., Wilner, D. J., & Qi, C. 2013, *ApJ*, 774, 16, doi: [10.1088/0004-637X/774/1/16](https://doi.org/10.1088/0004-637X/774/1/16)
- Sault, R. J., Teuben, P. J., & Wright, M. C. H. 1995, in *Astronomical Society of the Pacific Conference Series*, Vol. 77, *Astronomical Data Analysis Software and Systems IV*, ed. R. A. Shaw, H. E. Payne, & J. J. E. Hayes, 433
- Schlichting, H. E. 2014, *ApJ*, 795, L15, doi: [10.1088/2041-8205/795/1/L15](https://doi.org/10.1088/2041-8205/795/1/L15)
- Schneider, G., Grady, C. A., Hines, D. C., et al. 2014, *AJ*, 148, 59, doi: [10.1088/0004-6256/148/4/59](https://doi.org/10.1088/0004-6256/148/4/59)
- Schüppler, C., Löhne, T., Krivov, A. V., et al. 2015, *A&A*, 581, A97, doi: [10.1051/0004-6361/201525664](https://doi.org/10.1051/0004-6361/201525664)
- Sezestre, É., Augereau, J.-C., Boccaletti, A., & Thébault, P. 2017, *ArXiv e-prints*. <https://arxiv.org/abs/1707.09761>
- Strubbe, L. E., & Chiang, E. I. 2006, *ApJ*, 648, 652, doi: [10.1086/505736](https://doi.org/10.1086/505736)



- The Astropy Collaboration,  
Price-Whelan, A. M., Sipőcz, B. M.,  
et al. 2018, ArXiv e-prints.  
<https://arxiv.org/abs/1801.02634>
- Thébault, P. 2009, A&A, 505, 1269,  
doi: [10.1051/0004-6361/200912396](https://doi.org/10.1051/0004-6361/200912396)
- Thébault, P., & Augereau, J.-C. 2007,  
A&A, 472, 169,  
doi: [10.1051/0004-6361:20077709](https://doi.org/10.1051/0004-6361:20077709)
- Van Der Walt, S., Colbert, S. C., &  
Varoquaux, G. 2011, Computing in  
Science & Engineering, 13, 22
- Wang, J. J., Graham, J. R., Pueyo, L.,  
et al. 2015, ApJL, 811, L19,  
doi: [10.1088/2041-8205/811/2/L19](https://doi.org/10.1088/2041-8205/811/2/L19)
- Wetherill, G. W., & Stewart, G. R. 1993,  
Icarus, 106, 190,  
doi: [10.1006/icar.1993.1166](https://doi.org/10.1006/icar.1993.1166)
- White, S. M. 1996, in Cool stars; stellar  
systems; and the sun : 9 : Astronomical  
Society of the Pacific Conference  
Series, volume 109; Proceedings of the  
9th Cambridge workshop; held 3-6  
October 1995 in Florence; Italy; San  
Francisco: Astronomical Society of the  
Pacific (ASP); —c1996; edited by  
Roberto Pallavicini and Andrea K.  
Dupree, p.21, Vol. 109, 21
- Williams, J. P., & Cieza, L. A. 2011,  
ARA&A, 49, 67, doi: [10.1146/  
annurev-astro-081710-102548](https://doi.org/10.1146/annurev-astro-081710-102548)
- Wyatt, M. C. 2008, ARA&A, 46, 339,  
doi: [10.1146/annurev.astro.45.051806.  
110525](https://doi.org/10.1146/annurev.astro.45.051806.110525)
- Wyatt, M. C., & Dent, W. R. F. 2002,  
MNRAS, 334, 589,  
doi: [10.1046/j.1365-8711.2002.05533.x](https://doi.org/10.1046/j.1365-8711.2002.05533.x)